Pure Appl. Geophys. 173 (2016), 3935–3953

DOI 10.1007/s00024-016-1345-5

Pure and Applied Geophysics

Time–Frequency Characteristics of Tsunami Magnetic Signals from Four Pacific Ocean Events

N. R. Schnepf,[1,2] C. Manoj,[1,2] C. An,[3] H. Sugioka,[4] and H. Toh[5]

Abstract—The recent deployment of highly sensitive seafloor magnetometers coinciding with the deep solar minimum has provided excellent opportunities for observing tsunami electromagnetic signals. These fluctuating signals (periods ranging from 10–20 min) are generally found to be within $\pm \sim 1$ nT and coincide with the arrival of the tsunami waves. Previous studies focused on tsunami electromagnetic characteristics, as well as modeling the signal for individual events. This study instead aims to provide the time–frequency characteristics for a range of tsunami signals and a method to separate the data's noise using additional data from a remote observatory. We focus on four Pacific Ocean events of varying tsunami signal amplitude: (1) the 2011 Tohoku, Japan event (M9.0), (2) the 2010 Chile event (M8.8), (3) the 2009 Samoa event (M8.0) and, (4) the 2007 Kuril Islands event (M8.1). We find possible tsunami signals in high-pass filtered data and successfully isolate the signals from noise using a cross-wavelet analysis. The cross-wavelet analysis reveals that the longer period signals precede the stronger, shorter period signals. Our results are very encouraging for using tsunami magnetic signals in warning systems.

Key words: Tsunamis, marine electromagnetics, electromagnetic induction, tsunami warning systems, cross-wavelet analysis.

1. Introduction

Earth's oceans behave as a conducting fluid moving through Earth's magnetic field thereby inducing electric fields, electric currents, and secondary magnetic fields which have all been detected by ground, seafloor, and satellite measurements (Larsen 1968; Cox et al. 1971; Sanford 1971; Chave et al. 1989; Tyler et al. 2003; Maus and Kuvshinov 2004). Specific ocean processes such as tides (Larsen 1968; Tyler et al. 2003; Maus and Kuvshinov 2004; Malin 1970; McKnight 1995; Schnepf et al. 2014) and currents (Cox et al. 1971; Larsen and Sanford 1985; Larsen 1991) produce measurable electromagnetic fields. In 1971, Larsen predicted that tsunamis would also produce measurable magnetic fields and recent predictive work suggests that tsunami magnetic fields may provide useful directional information for warning systems (Tyler 2005; Toh et al. 2011; Minami et al. 2015). There has also been much recent progress in detecting tsunami magnetic signals, especially from larger events such as the 2011 Tohoku, Japan tsunami and Chile's 2010 tsunami (Toh et al. 2011; Thomson et al. 1995; Manoj et al. 2011; Utada et al. 2011; Ichihara et al. 2013; Klausner et al. 2014; Sugioka et al. 2014; Zhang et al. 2014; Tatehata et al. 2015).

Tsunamis travel with a dispersive phase velocity,

$$c = \sqrt{\frac{g\lambda}{2\pi}\tanh\frac{2\pi H}{\lambda}}, \tag{1}$$

where g is gravity, λ is the tsunami wavelength, and H is the local water depth. For earthquakes with $M > 8$, the tsunami's wavelength is on the order of tens to hundreds of kilometers, easily exceeding the depth of the ocean. Consequently, to a first order approximation the speed of the tsunami follows the shallow water equation, $c = \sqrt{gH}$, enabling tsunamis to travel at high speeds. For instance, assuming an ocean depth of 4 km, the tsunami will travel at ~ 200 m s^{-1}. The particles within tsunamis, however, do not travel nearly as fast: generally particles in the deep ocean have a speed of 1–10 mm s^{-1}.

[1] University of Colorado at Boulder, CIRES, Boulder, CO, USA. E-mail: neesha.schnepf@colorado.edu
[2] National Centers for Environmental Information, National Oceanic and Atmospheric Administration, Boulder, CO, USA.
[3] School of Civil and Environmental Engineering, Cornell University, Ithaca, NY, USA.
[4] Department of Planetology, Kobe University, Kobe, Japan.
[5] Data Analysis Center for Geomagnetism and Space Magnetism, Kyoto University, Kyoto, Japan.

Fortunately, the motion within a tsunami is coherent enough to produce observable electromagnetic fields by coupling with the geomagnetic main field's downward component, F_Z.

Sanford (1971) laid the theoretical groundwork of relating ocean flow to its electromagnetic fields, enabling a single ocean-bottom magnetometer station to provide data on a tsunami's local velocity components and angle of propagation. That same year, Cox et al. (1971) predicted the amplitude of the magnetic fields induced by a tsunami with a sea surface wave height of 20 cm passing through the Earth's vertical main field of 40,000 nT. While Sanford (1971) chose to ignore magnetic induction (a reasonable assumption when the tsunami phase velocity is approximately <10 m/s), Cox et al. (1971)'s work fully considered self-induction within a layered earth configuration. He found that such tsunamis would induce magnetic fields between 0.7–1.15 nT—a small but detectable signal. More recently, Tyler (2005) determined a relationship between the tsunami's induced vertical magnetic field b_z and its sea-surface displacement η using the long-wavelength assumption:

$$\frac{b_z}{F_z} = \frac{c}{c_s}\frac{\eta}{H}e^{-\kappa z}, \tag{2}$$

where F_z is the vertical component of the Earth's main field, H is the ocean depth, κ is the wave number vector describing the horizontal variation, z is the vertical position (positive downwards in our application), c is the tsunami's long wavelength non-dispersive surface gravity wave and c_s is a complex scaling speed, such that $c_s = c + 2iK/H$ where K is magnetic diffusion coefficient. The magnetic diffusion coefficient K is comprised of the magnetic permeability μ and the electrical conductivity σ of the medium (for our case, seawater) such that $K = (\mu\sigma)^{-1}$. Vacuum magnetic permeability is $\mu_0 = 4\pi \times 10^{-7}$ N A^{-2} and the mean electrical conductivity of seawater is $\sigma_0 = 3.2$ S/m. Equation 2 greatly simplifies the study of tsunamis, and has been used to predict the tsunami sea-surface displacement from tsunami magnetic signals (Minami et al. 2015; Ichihara et al. 2013; Zhang et al. 2014).

Most studies that have succeeded in detecting tsunami electromagnetic signals have been for events of M8.8 or larger (Manoj et al. 2011; Utada et al. 2011; Ichihara et al. 2013; Klausner et al. 2014; Sugioka et al. 2014; Zhang et al. 2014). The first study to look at smaller events was by Toh et al. (2011). They used a seafloor magnetometer station in the Northwestern Pacific (station denoted as 'NWP'; shown in Fig. 1) to analyze tsunami signals from the 2006 M8.3 and 2007 M8.1 Kuril Islands earthquakes. They found that while the tsunami signals were not detected at land magnetometer stations, the Northwestern Pacific (NWP) ocean bottom electromagnetic (OBEM) station registered a significant unipolar variation (i.e. a variation similar to a positive or negative impulse) in the horizontal amplitudes, as well as a bipolar variation (i.e. a variation similar to having an impulse immediately followed by an impulse of opposite direction) of the vertical field's magnitude with the passing of the tsunami.

The Gutenberg–Richter law relating an earthquake's magnitude and frequency has existed in various forms since 1956 (Gutenberg and Richter 1956) and it is generally accepted that lower magnitude events occur much more frequently than higher magnitude ones. While these lower magnitude events are relatively less violent, they still cause much grief. In the decade of 2005–2015, over 1500 people were killed by tsunamis resulting from earthquakes of magnitude smaller than M8.5 and damages of at least 294 million dollars were also incurred (NOAA 2015). Identifying signals from events smaller than M8.5 is necessary to better characterize tsunami magnetic signals and possibly incorporate them in warning systems. As discussed by Utada et al. (2011), large tsunamis produce a wave height great enough to disturb the ionosphere via delayed atmospheric gravity waves, thereby ensuring tsunami-caused magnetic signals may be detected at land stations (such as those used in their study). However, smaller tsunamis do not create such atmospheric disturbances and because their strongest signals are limited to just the ocean and conductive sediments, the signals from these smaller tsunamis cannot be sensed by land stations. Both Toh et al. (2011) and Sugioka et al. (2014) instead used seafloor magnetometer stations to detect tsunami electromagnetic signals. In each study, they found a clear signal in the vertical magnetic field data. Since these observational studies, Minami et al.

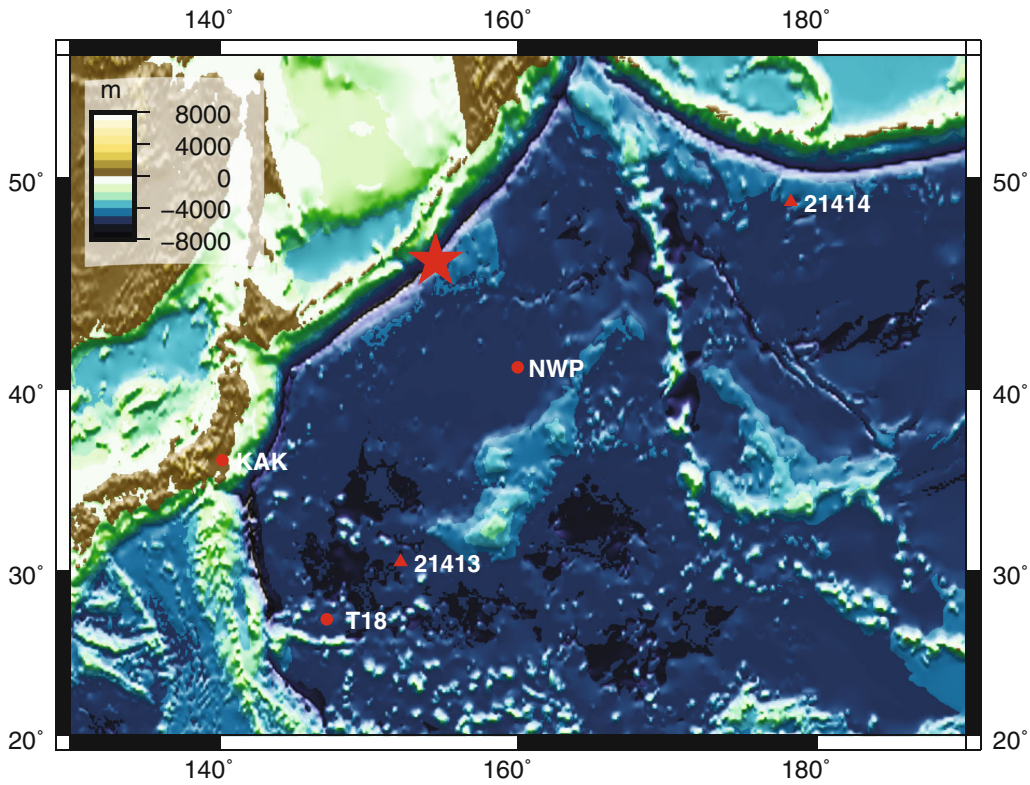

Figure 1
A bathymetry map showing magnetometer stations NWP, T18 and KAK (*red circles*), as well as the DART buoys 21413 and 21414 (*red triangles*). The *red star* denotes the epicenter of the 2007 Kuril Islands earthquake

(2015) classified tsunami electromagnetic signals into three scenarios based on ocean depth, finding tsunami magnetic signals in the deep ocean may precede the water wave arrival by as much as 18 % of the tsunami's period. These studies suggest magnetic field data may be more effective for tsunami detection in warning systems than pressure methods.

This study's aim was to detect tsunami magnetic signals from earthquakes ranging from M8.0–9.0 and analyze their time–frequency characteristics by producing a method to separate the data's noise using additional data from a remote observatory. The following section discusses this study's focus events and magnetometer stations. Section 3 describes the numerical simulation for tsunami water elevation used to estimate the tsunami's travel time and maximum magnetic field amplitude. Section 4.1 discusses the data processing and Sect. 4.2 describes our method of using a cross-wavelet analysis to isolate the tsunami magnetic signals from other outside sources. The results of each of these methods are discussed in Sect. 5 and we conclude with a summary and outlook.

2. The Data and Focus Tsunami Events

This study focused on four events varying in magnitude: (1) the January 13 2007 Kuril Islands event (M8.1), (2) the September 29 2009 Samoa event (M8.0), (3) the February 27 2010 Chile event (M8.8) and (4) the March 11 2011 Tohoku, Japan event (M9.0). Table 1 shows which magnetometer stations were used for each event, as well as the location of the earthquake origin, and the daily geomagnetic Ap index for each event (Denig 2015). With the exception of the 2011 Japan event, all of the events occurred on geomagnetically quiet days. The

Table 1

The focus tsunami events of this study and the stations with corresponding data

Origin	Data sets	Date	Lat.	Lon.	EQ. M	Ap index
Kuril Islands	T18, NWP, KAK[a]	1/13/2007 4:23:21.1	46.24°N	154.52°E	8.1	0
Samoa	SOC1–9, HON[a]	9/29/2009 17:48:10.9	15.489°S	−172.095°E	8.0	1
Chile	SOC1–9, HON[a]	2/27/2010 6:34:11.5	36.122°S	−72.898°E	8.8	1
Japan	CBI, MMB[a]	3/11/2011 5:46:24.1	38.297°N	142.372°E	9.0	37

The latitude and longitude of the earthquake's origin are given, as is the earthquake's magnitude (NOAA 2015) and the Ap index of the event's day (Denig 2015)

[a] A land station used as the remote station for the cross-wavelet analysis

2007 Kuril Islands event was previously studied by Toh et al. (2011), and we were curious how well other OBEMs could identify the event's signals. The 2011 Tohoku, Japan and 2010 Chile events are well studied so they were also well suited for testing our methods.

We used data from Pacific ocean-bottom electromagnetometer (OBEM) observatories (shown in Figs. 1, 2), as well as Pacific (Fig. 3) and Japanese (Figs. 1, 4) INTERMAGNET and Japan Meterological Agency (JMA) stations. The stations' latitudinal/longitudinal coordinates and depths are shown in Table 2. The OBEMs provide the most ideal data set for this study: their location on the seafloor provides greater exposure to all the tsunami produced fields (the toroidal field is restricted to within the ocean and conductive seafloor sediments), ensuring a higher signal-to-noise ratio than at a land station. Each of the OBEMs has red background noise such

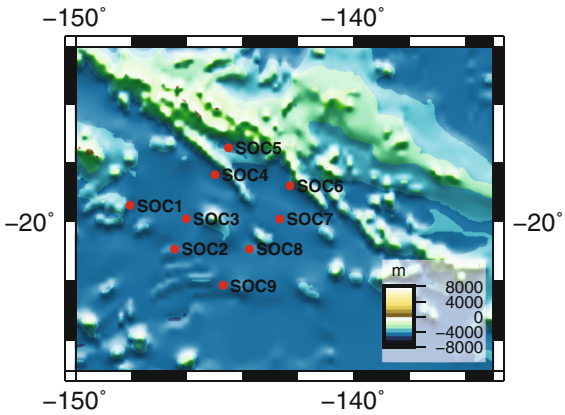

Figure 2
A bathymetry map showing the SOC1-9 ocean-bottom magnetometer network

that, with the exception of station SOC6 for both events (2) and (3), and SOC9 for event (2), the background noise level in the period range expected for tsunamis is well under 1 nT. These three exceptions have background noise ranging from 1.4–1.5 nT within this period range. An example of the typical red background noise is shown in Fig. 5 using station SOC1 (September–October 2009) with a dashed vertical line included to denote a period of 15 min. Although the background noise is well below 1 nT at most of the stations, as will be discussed Sect. 3.1, this level of noise is generally similar in magnitude to any expected tsunami signals necessitating additional data filtering techniques to ensure minimization of noise and extraction of the tsunami signal.

Station T18 collected data every minute for ~ 1 year using a vector fluxgate magnetometer to determine the northward (X), eastward (Y) and downward (Z) components as part of a study to understand the deep geoelectrical structure of the ocean-subsurface (Baba et al. 2010). The nine SOC stations (SOC1-9) were similarly employed for magnetotelluric purposes and collected vector data every minute (Suetsugu et al. 2012). Station NWP collects data every 2 min with resolutions of 0.01 nT and 0.64 mV/m for the magnetic and electric fields, respectively (Toh et al. 2011, 2006). The attitude of the OBEMs is initially determined and each of the stations monitor changes in tilt to accommodate for movements of the OBEM platform.

Besides these seafloor stations, the JMA and INTERMAGNET station Kakioka (KAK) was used to produce the cross-weight matrix in the cross-wavelet analysis for the 2007 Kuril Islands event and the station Memambetsu (MMB) was used for the

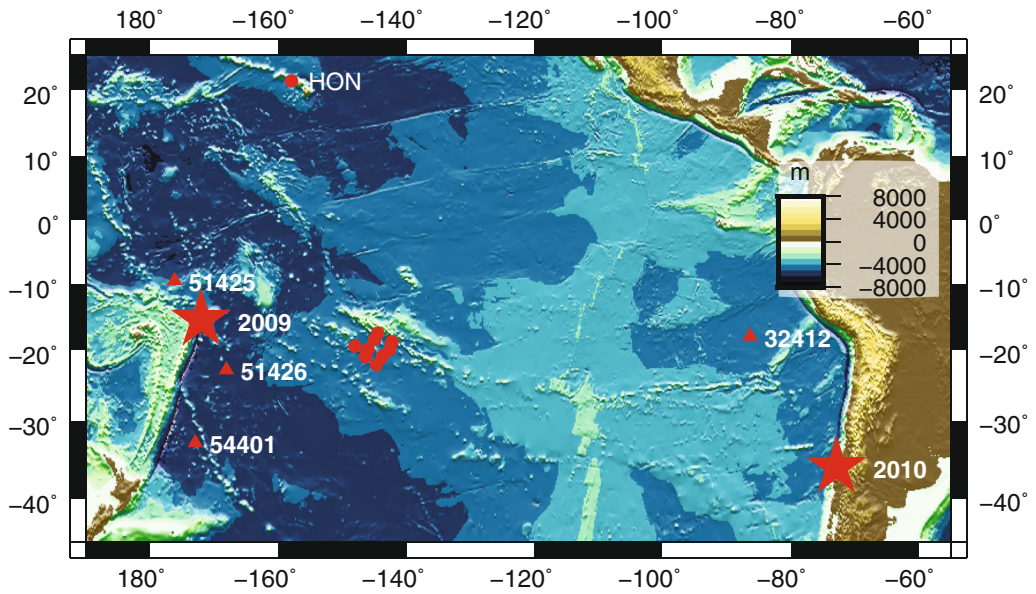

Figure 3
A bathymetry map showing the SOC1-9 ocean-bottom magnetometer network and the INTERMAGNET station HON (*red circles*), as well as the DART buoys 54401, 51426, 51425 and 32412 (*red triangles*). The epicenters of the 2009 Samoa and 2010 Chile earthquakes are labelled with *red stars*

2011 Tohoku, Japan event (see Sect. 4.2). We also used JMA's station Chichijima (CBI) for the 2011 Tohoku, Japan event's local data. The U.S. Geological Survey and INTERMAGNET Honolulu station (HON) was used as the remote station for the cross-wavelet analysis with the SOC stations for the 2009 Samoa and 2010 Chile events.

3. *Numerical Simulation of the Tsunami Water Elevation*

The Cornell Multi-grid Coupled Tsunami model (COMCOT) was used to predict the arrival time of the leading tsunami wave at NWP, T18 and CBI because these magnetometer stations are not accompanied by a pressure gauge or tide gauge. The SOC stations all included pressure gauges, so we were able to compare COMCOT's results with pressure data, as well as use COMCOT to estimate the size of the expected tsunami magnetic signal (discussed in the following section). Besides estimating the arrival of each tsunami at the respective OBEMs, we also estimated the arrival at deep-ocean assessment and reporting of tsunamis (DART) buoys or coastal tide-gauge stations to check the simulation's estimated time of arrival (ETA) with the tsunami's actual arrival time at the buoy or tide-gauge (shown in Table 3).

This study's simulations used a 2-arc min bathymetry grid provided through (GEBCO 2013) and a time step of two seconds. For the 2007 Kuril Islands event, the focal mechanisms of Fujii and Satake (2008) were used; for the 2009 Samoa event the mechanisms from Fujii and Satake (2009) were used; for the 2010 Chile event, we used the mechanisms of Yue et al. (2014); and for the 2011 Tohoku, Japan event we used the mechanisms discussed in An (2015). For more details on COMCOT, see "Appendix".

In general, COMCOT's tsunami ETA matches within $\sim$2–8 min of the measured tsunami time of arrival at DART buoys/tide-gauge stations and SOC8 (shown in Table 3). The largest discrepancies were $\sim$12 min for simulating the arrival at DART buoy 21414 for the 2007 Kuril Islands event and the arrival of the 2010 Chile tsunami at SOC8. Meanwhile, the smallest discrepancy was 4s for the 2011 Tohoku, Japan event at the DART buoy 21419. The discrepancies between COMCOT's results and the actual

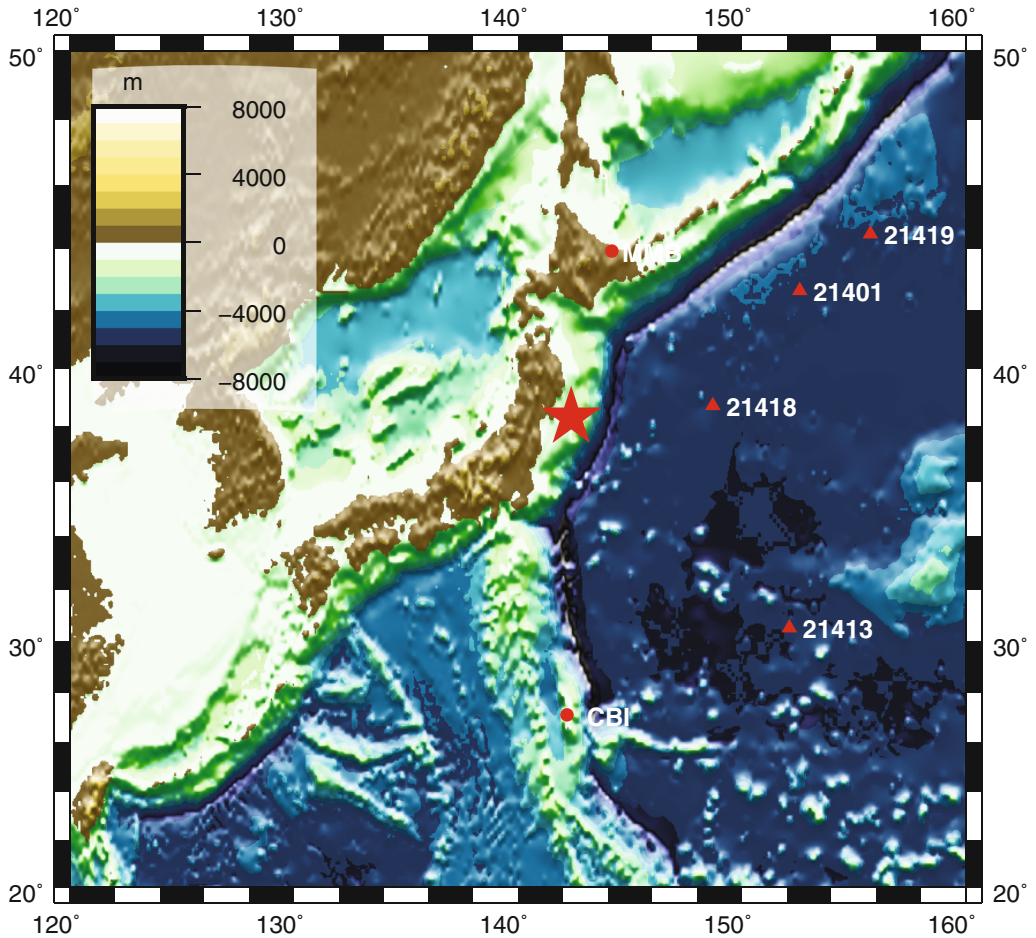

Figure 4
A bathymetry map showing the magnetometer stations (*red circles*) used for analyzing the 2011 Tohoku, Japan event and the event's epicenter (*red star*), as well as the DART buoys 21419, 21401, 21418 and 21413 (*red triangles*)

water wave arrival may be due to inaccurate focal mechanisms.

3.1. *Using COMCOT to Predict the Expected Magnetic Field Signal*

The relation given in Eq. 2 was used to estimate the induced magnetic field produced by the 2007 Kuril Islands, 2009 Samoa and 2010 Chile events at the OBEMs. The velocities and sea surface heights were predicted by COMCOT and the scaling factor, c_s, was assumed to be negligibly different from the wave speed ($\frac{c}{c_s} \approx 1$). The exponential term in Eq. 2 was also simplified to 1 (Tyler 2005; Zhang et al. 2014).

The expected magnetic field (b_z from Eq. 2) for the Kuril Islands event reaches 0.08 nT at T18 and 0.4153 nT at NWP. For the 2009 Samoa event, across SOC1-9 the expected maximum magnetic field amplitude ranges from 0.1278 nT at SOC6 to 0.1961 nT at SOC1. For the 2010 Chile event, also across SOC1-9, the expected maximum magnetic field amplitude ranges from 0.4295 nT at SOC8 to 0.4947 nT at SOC2. The spread in expected magnetic field amplitude is most likely due to local bathymetry variations, however local variations in electrical conductance may also affect the observed tsunami's magnetic signal. Regardless, all of the expected magnetic signals are smaller than the background noise for the tsunami-relevant period range.

Table 2

The electromagnetic stations' locations and the average Z magnitude for the station over the data's time span

Station	Lat.	Lon.	Elevation (m)	Z (nT)
Baba et al. (2010)				
T18	27.14°N	147.17°E	−5594	2.3687×10^4
Toh et al. (2006, 2011)				
NWP	41.102°N	159.963°E	−5580	3.5843×10^4
Suetsugu et al. (2012) and Sugioka et al. (2014)				
SOC1	19.4682°S	148.0498°E	−4427	2.0906×10^4
SOC2	20.9561°S	−146.4423°E	−4772	2.2857×10^4
SOC3	19.9286°S	−146.0260°E	−4656	1.9559×10^4
SOC4	18.4281°S	−144.9878°E	−4478	1.9138×10^4
SOC5	17.5012°S	−144.5069°E	−4049	1.8161×10^4
SOC6	18.8055°S	−142.2961°E	−4508	1.9014×10^4
SOC7	19.9405°S	−142.6682°E	−4490	1.9925×10^4
SOC8	20.9548°S	−143.7570°E	−4806	2.0420×10^4
SOC9	22.1675°S	−144.6965°E	−4540	2.2824×10^4
INTERMAGNET				
KAK	36.23°N	140.18°E	36	3.5400×10^4
MMB	43.91°N	144.19°E	42	3.9706×10^4
CBI	27.096°N	142.185°E	155	2.4961×10^4
HON	21.3°N	−158°E	4	2.1271×10^4

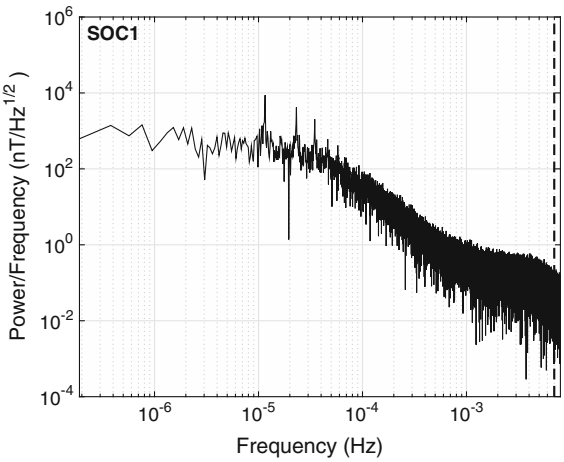

Figure 5
An example of the red background noise typical for the magnetometer stations, this is an amplitude spectral density of station SOC1 for two months of data (September–October 2009). The *dashed vertical line* (on the *far right*) denotes the frequency corresponding to a period of 15 min

4. Concurrent Ocean Bottom Magnetic Data

4.1. Data Processing

The predominant signal of the time series is that of daily variation (forced by the thermally driven ionospheric dynamo) with intermittent spikes due to magnetic storms. To remove these extraneous signals, the data underwent a high pass butterworth filter where signals with periodicities of 30 min or greater were removed. Previously observed tsunami generated magnetic signals (Toh et al. 2011; Manoj et al. 2011; Utada et al. 2011) showed quasi-sinusoidal fluctuations with typical periods of 10–20 minutes. Hence, this method limits our analysis to this period.

The results of this filtering are shown in Fig. 8 for the 2007 Kuril Islands event, Fig. 7 for the 2009 Samoa and 2010 Chile events, and Fig. 6 for the 2011 Tohoku, Japan event. For the 2007 Kuril Islands event at T18, the filtered vertical component shows very small amplitudes within ±0.04 nT for the duration of each event. This is less than the expected b_z of 0.08 nT. While T18 does not show any clear signals denoting the arrival of the 2007 Kuril Islands tsunami, NWP does. Interestingly, the maximum amplitudes for NWP are ∼1.5 nT—much larger than the 0.4153 nT estimated using (Tyler 2005)'s relation and much larger than the background noise.

At the SOC stations, the magnetic field amplitudes are again much larger than those expected. Interestingly, SOC6 has the smallest expected b_z for the 2009 Samoa event and its data's noise is comparable in amplitude to any possible tsunami

Table 3

The tsunamis' estimated time of arrival (ETA) calculated from the COMCOT simulation for tide-gauges and DART buoys sensitive to each event

2007 Kuril Islands event—focal mechanisms from Fujii and Satake (2008)		
DART buoy 21413	01-13-2007 06:27:03	0.02487
Simulation for 21413	01-13-2007 06:24:03	0.02176
DART buoy 21414	01-13-2007 06:36:03	0.02925
Simulation for 21414	01-13-2007 06:24:49	0.03428
2009 Samoa event—focal mechanisms from Fujii and Satake (2009)		
DART 51425	09-29-2009 18:54:00	0.02751
Simulation for 51425	09-29-2009 18:52:03	0.04648
DART 51426	09-29-2009 19:00:00	0.06337
Simulation for 51426	09-29-2009 18:52:10	0.06593
DART 54401	09-29-2009 20:01:58	0.01810
Simulation for 54401	09-29-2009 20:03:46	0.02563
SOC8	09-29-2009 21:44:30	
Simulation for SOC8	09-29-2009 21:42:46	
2010 Chile event—focal mechanisms from Yue et al. (2014)		
DART 32412	02-27-2010 09:49:02	0.1964
Simulation for 32412	02-27-2010 09:48:44	0.2005
DART 51426	02-27-2010 18:30:02	0.0093
Simulation for 51426	02-27-2010 18:33:08	0.0180
DART 54401	02-27-2010 18:12:02	0.0152
Simulation for 54401	02-27-2010 18:20:26	0.0132
SOC8	02-27-2010 16:35:46	
Simulation for SOC8	02-27-2010 16:43:08	
2011 Japan event—focal mechanisms from An (2015)		
DART 21413	03-11-2011 07:07:01	0.8060
Simulation for 21413	03-11-2011 07:04:01	0.7689
DART 21401	03-11-2011 06:53:01	0.6177
Simulation for 21401	03-11-2011 06:51:09	0.5116
DART 21418	03-11-2011 06:19:01	1.8880
Simulation for 21418	03-11-2011 06:19:13	1.1420
DART 21419	03-11-2011 07:16:01	0.5700
Simulation for 21419	03-11-2011 07:15:57	0.4150

The last column denotes the observed and estimated wave height (m). For the 2009 Samoa event and 2010 Chile event, we include a comparison of COMCOT's results to the arrival time obtained from SOC8's pressure data

signal making the detection of such a signal unclear. For the 2010 Chile event, SOC8 was expected to have the smallest b_z, but again SOC6 is the noisiest without any clear tsunami signal. All the other stations have a clear signal coinciding with the tsunami arrival. Figure 7 shows the results for SOC1, SOC2, SOC6 and SOC9.

For the 2011 Tohoku, Japan event, CBI's horizontal component (ranging from about ± 10 nT) does not have a clear signal with the arrival of the tsunami, but the vertical component (ranging from ± 2 nT) does show strong variations with the tsunami ETA (Fig. 6).

The discrepancies between amplitudes revealed via a high pass filter and the estimation in the previous section may be due to magnetospheric noise of similar periodicity to tsunamis, variations in the scaling factor c_s, local conductivity or Eq. 2's exponential term, errors in the tsunami focal models used or the effect of dispersion since COMCOT cannot handle dispersive tsunamis. Additionally, the signals concurrent with the tsunami's ETA for the SOC stations are all either similar in magnitude or smaller than the background noise in the tsunami-relevant period range for each station's power spectra. A cross-wavelet analysis (discussed in the next section) is needed to rule out magnetospheric noise and minimize background instrument noise.

4.2. Signals from a Cross-Wavelet Analysis

While a Fourier transform is often used to extract frequency components from a signal, it is not

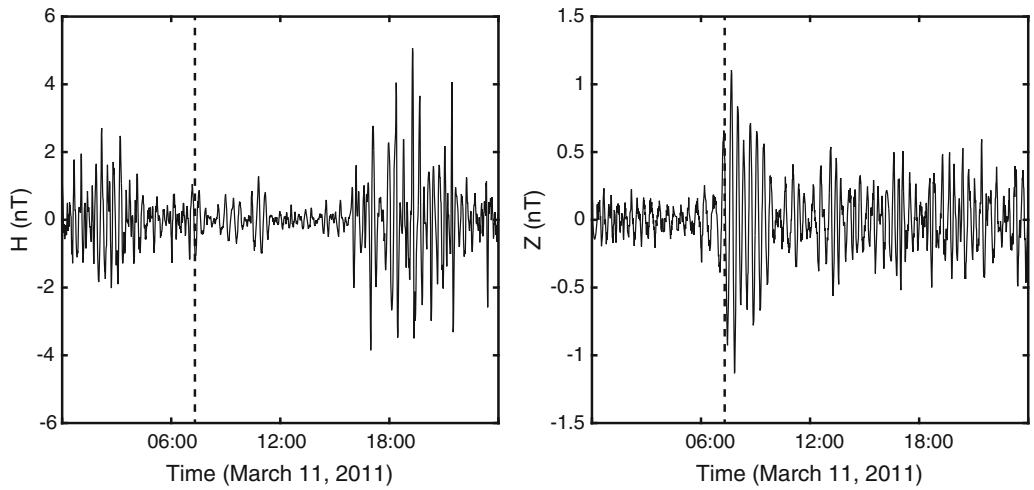

Figure 6
The high pass filtered time series for the horizontal (*left*) and vertical (*right*) field component at Chichijima (CBI) in temporal proximity to the tsunami's estimated time of arrival (*dashed line*). The given date and time are in UTC

useful for short-lived phenomena such as the signal of a passing tsunami. As summarized by Newland (1993), this arises because the Fourier transform extends over all time ($-\infty$ to ∞), so it only provides an average over the entire length of the signal, $f(t)$. If at some point in the lifetime of $f(t)$ there is an anomalous event, it will contribute to the calculated Fourier transform, $\hat{F}(\omega)$, but its location on the time axis will be lost. There will be no way of knowing if the value of $\hat{F}(\omega)$ at a particular ω is due to frequencies present throughout the signal $f(t)$ or if it is due to occurrences during a select period of time within $f(t)$.

Instead, a wavelet analysis was done on each component of the magnetic field data at each station to extract both the frequency components of the data and their time dependency. Wavelet analyses have been previously applied to tsunami data from deep-ocean buoys (González and Kulikov 1993), coastal water level stations (González et al. 1995; Mofjeld et al. 1997; Titov et al. 2005; Nagarajan et al. 2006; Rabinovich et al. 2006; Rabinovich and Thomson 2007), DART buoy data (Tang et al. 2008), and magnetometer data (Klausner et al. 2014; Mendes et al. 2005).

The analyzing function of a Fourier transform is $e^{i\omega t}$ and for a short-time Fourier transform the analyzing function is windowed becoming $w(t)e^{i\omega t}$. Unlike these Fourier methods, wavelet analyses use an analyzing function known as the mother wavelet (ψ) giving the following expression for the wavelet transform (Daubechies 1992; Liu 2000):

$$\tilde{F}(a,b) = \int_{-\infty}^{\infty} f(t)|a|^{-1/2}\psi^*\left(\frac{t-b}{a}\right)\mathrm{d}t. \qquad (3)$$

Here, a and b are the dilation and translation factors. The $|a|^{-1/2}$ term is from the normalization of the mother wavelet, which must also satisfy the following admissibility condition:

$$C_\psi = 2\pi \int \frac{\mathrm{d}\omega}{|\omega|}|\hat{\psi}(\omega)|^2 < \infty. \qquad (4)$$

This admissibility condition (Liu 2000; Grossmann and Morlet 1984) allows a data signal, $f(t)$, to be reconstructed from the wavelet $\psi_{ab}(t)$ and its corresponding wavelet transform $\tilde{F}(a,b)$ as:

$$f(t) = \frac{1}{C_\psi}\int_{-\infty}^{\infty}\mathrm{d}a\int_{-\infty}^{\infty}\mathrm{d}b\tilde{F}(a,b)\psi_{ab}(t)\frac{1}{a^2}. \qquad (5)$$

This reconstruction formula is known as the resolution of the identity (Grossmann and Morlet 1984; Liu 2000). To analyze data, the continuous wavelet transform (Eq. 3) may be discretized by respectively setting the dilation and translation factors to $a = 2^s$ and $b = \tau 2^s$ (Daubechies 1992; Liu 2000). This gives a mother wavelet of

$$\psi_{s\tau}(t) = 2^{-s/2}\psi(2^{-s}t - \tau) \qquad (6)$$

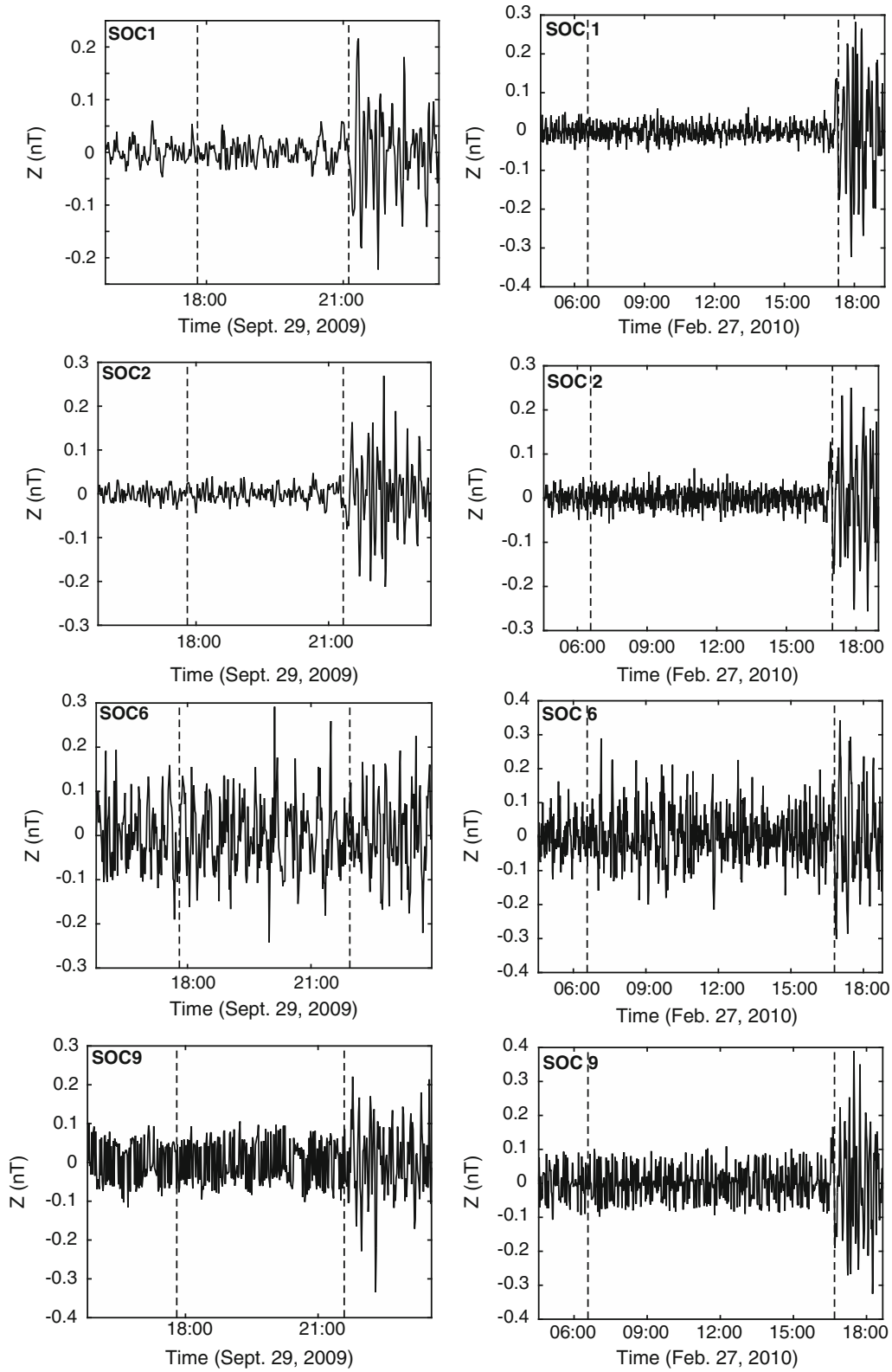
SOC1
SOC 1
SOC2
SOC 2
SOC6
SOC 6
SOC9
SOC 9
Z (nT)
18:00
21:00
06:00
09:00
12:00
15:00
18:00
Time (Sept. 29, 2009)
Time (Feb. 27, 2010)

◀Figure 7
The high pass filtered time series for the vertical field component in temporal proximity to the earthquake's time of origin (*first dashed line*) and the tsunami's estimated time of arrival (*second dashed line*). The left column is for the 2009 Samoa event and the right column is for the 2010 Chile event. Stations SOC6 and SOC9 were the noisiest two stations, whereas SOC1 and SOC2 are typical of the filtered quality for the other stations. The given date and time are in UTC

where s and τ are integers that represent frequency and time, respectively. Using this, the wavelet transform (Eq. 3) becomes

$$\tilde{F}(s,\tau) = \frac{1}{\sqrt{2^s}} \int_{-\infty}^{\infty} f(t)\psi^*\left(\frac{t}{2^s} - \tau\right) \mathrm{d}t. \qquad (7)$$

For each tsunami event and station's high pass filtered ocean bottom magnetometer data, we used this method with a continuous fourth-order Gaussian mother wavelet.

To verify that extraneous signals (such as those from the magnetosphere) were not being incorporated into the observed vertical component's data, we developed a cross-wavelet analysis between the horizontal components of the local station of interest and a land station further away. This method assumes that in the tsunami-relevant period range, magnetospheric signals are similar over large spatial scales so rather than solely use the local station's data, an additional land magnetometer station was incorporated to filter the wavelet analysis of the ocean-local station. The land station must be devoid of ocean signals so that the only temporally similar magnetic signals between it and the local station will be from non-oceanic sources or similar red background instrument noise. For this purpose, the land stations used were KAK (for the 2007 Kuril Islands event), MMB (for the 2011 Tohoku, Japan event), HON (for the 2009 Samoa and 2010 Chile events) and PPT (for the 2010 Chile event). Table 1 summarizes which stations were used in the cross-wavelet analysis.

To perform the cross-wavelet analysis, the magnetic data from both the land station's and the local seafloor or island station's horizontal components' time series (respectively H_L^t and H_O^t) first undergo a wavelet transform (denoted $\tilde{H}_{L,O}^{s,\tau}$, this is a $n \times m$ matrix of the amplitudes corresponding to different n frequencies (s) at each of the m time points (τ)). The resulting series then produce a matrix by multiplying $\tilde{H}_O^{s,\tau}$ by the complex conjugate of $\tilde{H}_L^{s,\tau}$:

$$H^{s,\tau} = \tilde{H}_O^{s,\tau} \tilde{H}_L^{*s,\tau}. \qquad (8)$$

The weight matrix $w^{s,\tau}$ is then produced by dividing the difference between the complex magnitude matrix of $H^{s,\tau}$ (i.e. $|H_k^{s,\tau}| = \sqrt{a_k^2 + b_k^2}$, if at index k have $H_k^{s,\tau} = a_k + ib_k$) and $|H^{s,\tau}|$'s absolute maximum value by the absolute maximum difference:

$$w^{s,\tau} = \frac{|H^{s,\tau}| - \max(|H^{s,\tau}|)}{\max(|H^{s,\tau}| - \max(|H^{s,\tau}|))}. \qquad (9)$$

The cross-wavelet analysis is then completed by multiplying $w^{s,\tau}$ and the absolute values of the ocean bottom's vertical component wavelet transform. This

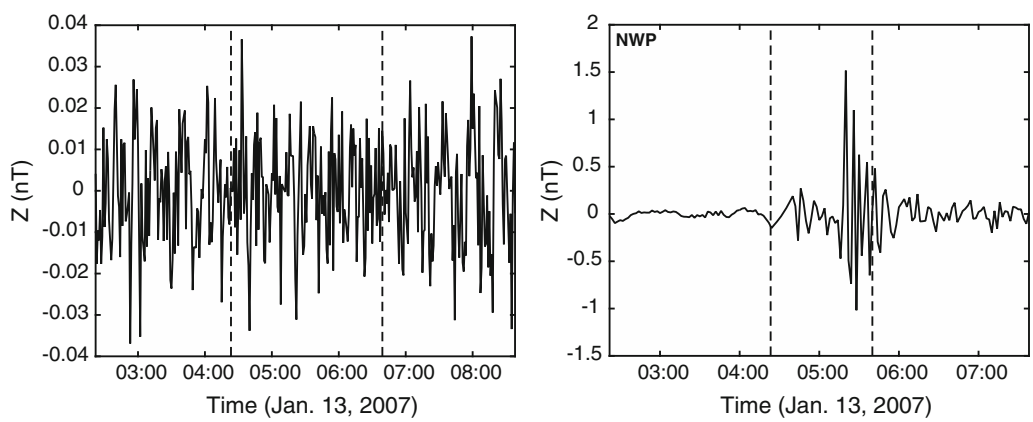

Figure 8
The high pass filtered time series for the vertical field component in temporal proximity to the earthquake's time of origin (*first dashed line*) and the tsunami's estimated time of arrival (*second dashed line*) for station T18 (*left*) and NWP (*right*). The given date and time are in UTC

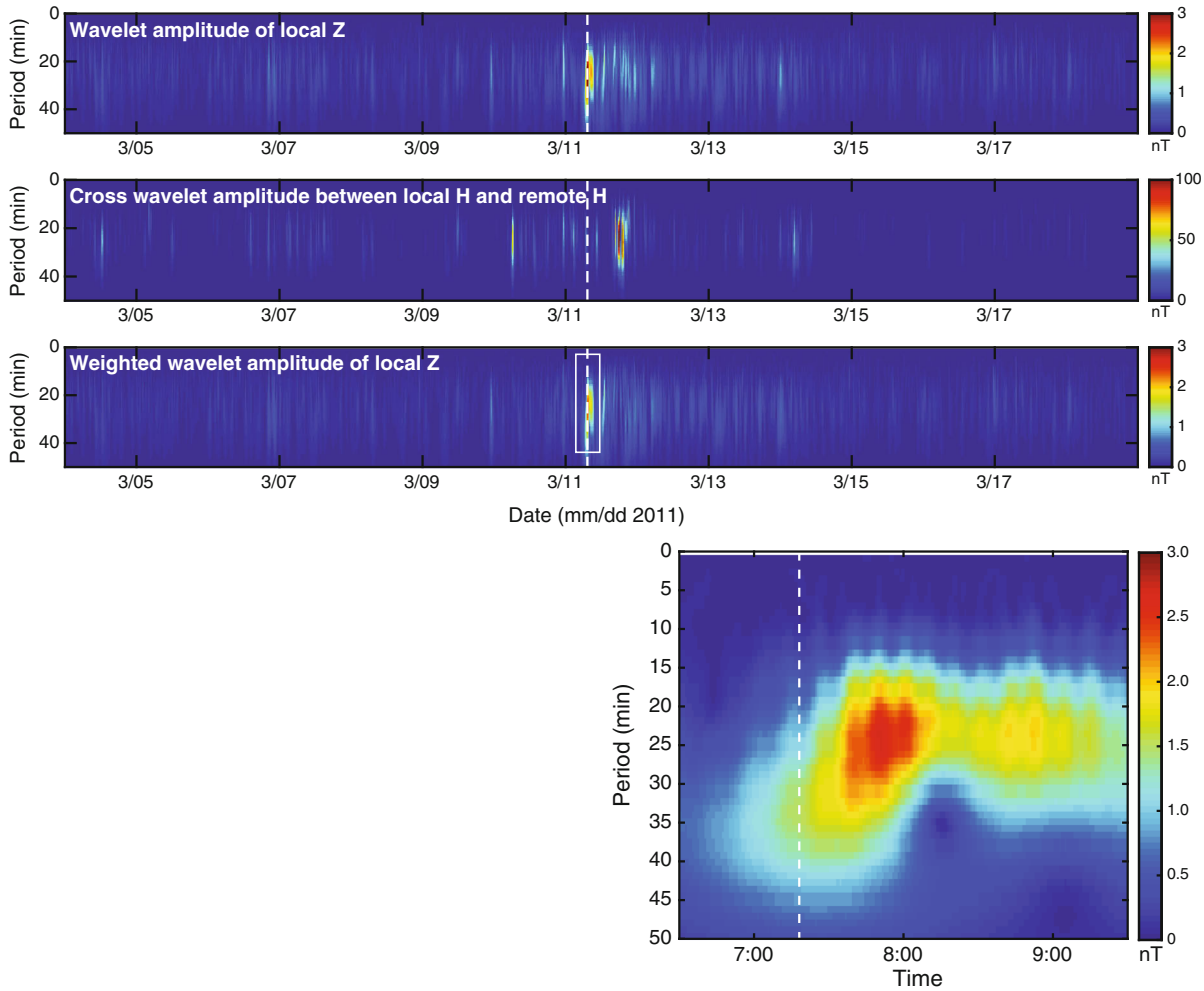

Figure 9
Results of the cross-wavelet analysis at CBI for the 2011 Tohoku, Japan event. Each step of the analysis is shown: (*top*) the local vertical wavelet periodogram at CBI, (*middle*) the cross-wavelet periodogram between the local and remote (MMB) horizontal components, and (*bottom*) the weighted wavelet periodogram for the local vertical component, where the *white box* denotes the region shown in the zoomed-in figure. The *white dashed line* marks the tsunami's estimated time of arrival and UTC time is used

down-weighs signals that occur at the same time at both of the stations, while also strengthening the events that occur uniquely at the ocean-local station.

The present study uses the cross-wavelet analysis between data collected at a local ocean site and a remote land site to reduce noise at the former site. This is different from Klausner et al.—their study similarly used the wavelet method on magnetometer data to study signals from the 2010 Chilean tsunami, however they computed the cross-correlation between the magnetometer periodogram and that of the tide/pressure gauge data. Unlike their method, our cross-wavelet analysis only uses magnetometer data so local pressure or tide gauges are not needed. Additionally, our method directly removes noise from the resulting wavelet periodograms.

5. Discussion

As a check for this method, we start by examining the cross-wavelet analysis for the largest event—the 2011 Tohoku, Japan tsunami's magnetic signal at CBI (shown in Fig. 9). While the original tsunami

signal is visible in the high-pass filtered data at CBI (right side of Fig. 6) and in a wavelet analysis of CBI's vertical component (top panel of Fig. 9), the method illustrates how to remove or diminish much of the noise. This is most easily seen by considering the days directly preceding the tsunami event: much of the noise has been dramatically reduced in the final results of the cross-wavelet analysis (bottom panel and bottom box of Fig. 9) and a strong signal concurrent with the tsunami's ETA is isolated.

The work of Tatehata et al. (2015) found a negative peak in Z occurring before 7:00 (UTC) and they named this peak the "first motion" as part of a claim that magnetic signals reached CBI 20 minutes before the tsunami water wave's arrival. However, as shown in Fig. 4 of their paper, their simulation failed to reproduce this first motion. Our results (this is especially evident in the bottom box of Fig. 9) revealed that only higher period, lower amplitude ($\sim$1 nT) magnetic signals preceded the arrival of the tsunami water wave; most of the signal either coincided or immediately followed the arrival of the tsunami water wave at CBI. The tsunami's dispersive phase velocity (given in Eq. 1) implies that longer periods will travel faster and this phenomenon is evident in the bottom box of Fig. 9 where the signal seems to be diagonally smeared upwards as shorter period signals arrive after longer period signals. Thus, we argue that their so-called "first-motion" may be due to the dispersive nature of the tsunami water wave and their simulation

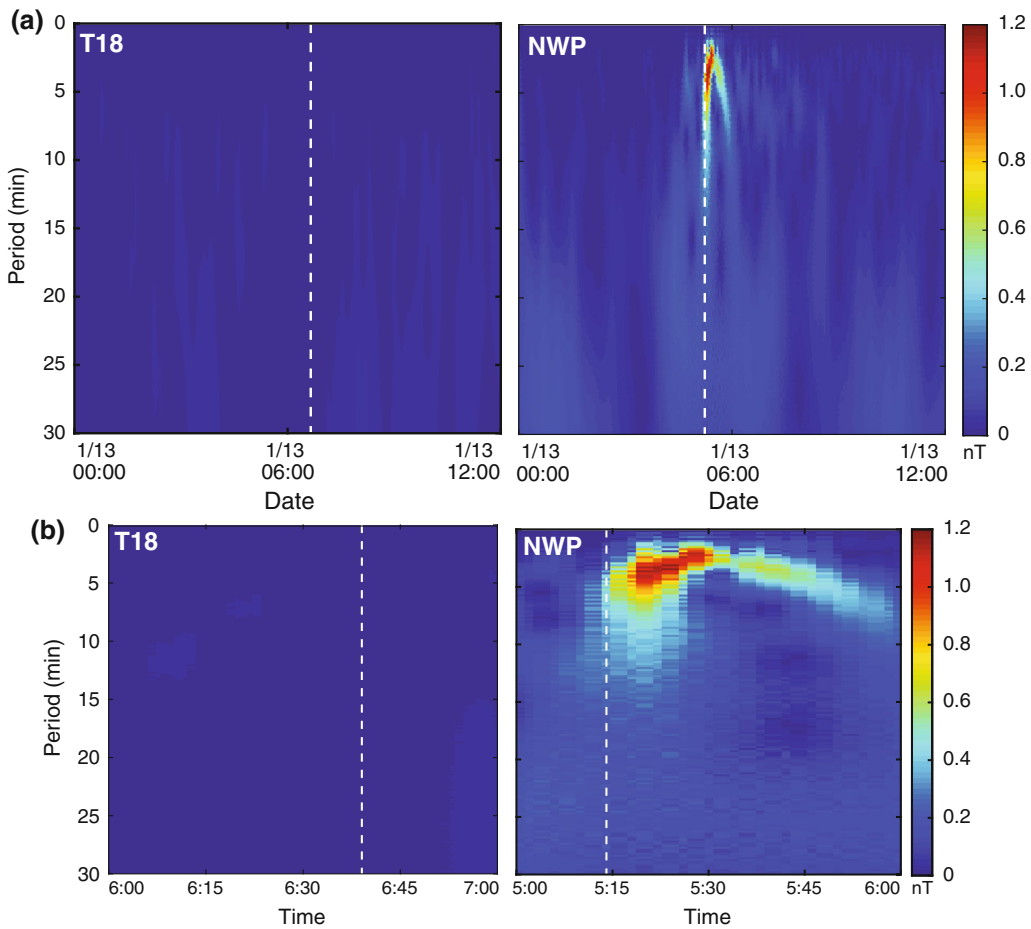

Figure 10
Results of the cross-wavelet analysis for the 2007 Kuril Islands event at T18 and NWP. The *white dashed line* marks the tsunami's estimated time of arrival and UTC time is used. The *top row* (**a**) shows the periodogram for the first 12 h of January 13, 2007, whereas the *bottom row* (**b**) focuses on the hour of the tsunami's arrival

may have failed to reproduce the first motion because (similar to the simulation method we used) it does not incorporate dispersion. However, the long gap between the strongest magnetic signals and the initial signals, as well as the periodogram's vertical smear along the period axis suggests there are non-linear influences beyond dispersion also at play.

Because land stations have a lower signal-to-noise ratio than OBEMs, we anticipated greater success for isolating tsunami signals and examining the time–frequency characteristics when applying this method on OBEM data and, with these hopes, employed this method to the OBEM data. The cross-wavelet analysis method successfully removed noise and isolated the tsunami signal in the OBEM data– only four stations out of the eleven considered across all the events proved too noisy to isolate a signal.

Shown in Fig. 10, the cross-wavelet analysis of NWP's data with KAK revealed a clear signal coinciding with the tsunami ETA for the 2007 Kuril Islands event. This signal had a maximum amplitude of 1.2 nT for periods near 4 min and occurred within 5–15 min of the tsunami's ETA (note that our analysis has a time resolution of 1 min and the tsunami's ETA may vary from the actual tsunami water wave arrival). Minami et al. (2015) predicted that for the ocean depth of this study's OBEMs, the tsunami electromagnetic fields correspond to the self-induction dominant case and the peak of b_z should precede the tsunami water wave arrival (η) by $\sim 0.07T$ where T is the tsunami's period. If the strongest period component for this event was about 4 min, then the b_z would be expected to arrive ~ 17 s ahead of η. If our simulated ETA is the true tsunami ETA, then this was not the case for this event. However, as shown in Table 3, COMCOT's ETA may be 2–12 min off from the actual arrival of η, so we cannot confirm whether Minami et al. (2015)'s prediction was validated for this event. Unlike NWP, as shown in Fig. 10a, T18 lacks any clear signals for this event. This is not surprising since the tsunami signals at T18 were expected to be dramatically smaller than the background noise (0.08 versus 0.4 nT). However, it is note worthy that besides lacking tsunami signals, the periodogram for this station hardly has any noise—another indicator that the cross-wavelet analysis is suitable for isolating tsunami signals, if they are present.

Figure 11 ▶
Results of the cross-wavelet analysis at the nine SOC stations for the 2009 Samoa event. The *white dashed line* marks the tsunami's estimated time of arrival and UTC time is used. **a** Each step of the analysis is shown: (*top*) the local vertical wavelet periodogram at SOC 7, (*middle*) the cross-wavelet periodogram between the local and remote (HON) horizontal components, and (*bottom*) the weighted wavelet periodogram for the local vertical component. **b** 2 h time windows of the weighted wavelet periodogram for the local vertical component at each SOC station

For the 2009 Samoa event, stations SOC1-4 and SOC7-8 show strong signals arriving concurrently or immediately after the tsunami's ETA with little noise preceding the tsunami's ETA (Fig. 11). As expected due to the dispersive nature of tsunamis, the longer period signals arrive a before the stronger, shorter period signals. Stations SOC5, SOC6 and SOC9 all were too noisy despite the cross-wavelet analysis so although there may seem to be signals coinciding with the tsunami's arrival, because there were many similar signals through the periodogram it is not clear if this local signal is the tsunami or other local circulation effects.

Unlike the 2009 Samoa event, for the larger 2010 Chile event every station shows a strong signal with the tsunami's ETA with little noise preceding it (Fig. 12). Similar to the 2009 Samoa event, the longer period signals precede the stronger, smaller period signals. These longer period signals in fact arrive before the tsunami's ETA faster than the ~ 0.07 lead-time (i.e. ~ 2 min) predicted by Minami et al. (2015).

6. Summary and Conclusions

Through a cross-wavelet analysis using a local (seafloor or island) magnetometer station and a remote land station (which cannot have any tsunami signals), we were generally able to effectively remove atmospheric noise and isolate local signals revealing tsunami generated magnetic signals. Our results confirm that longer period signals arrive faster than shorter period signals—a feature that may be useful, albeit challenging since the shorter period signals tend to be stronger, for incorporation into tsunami warning systems. These results are very

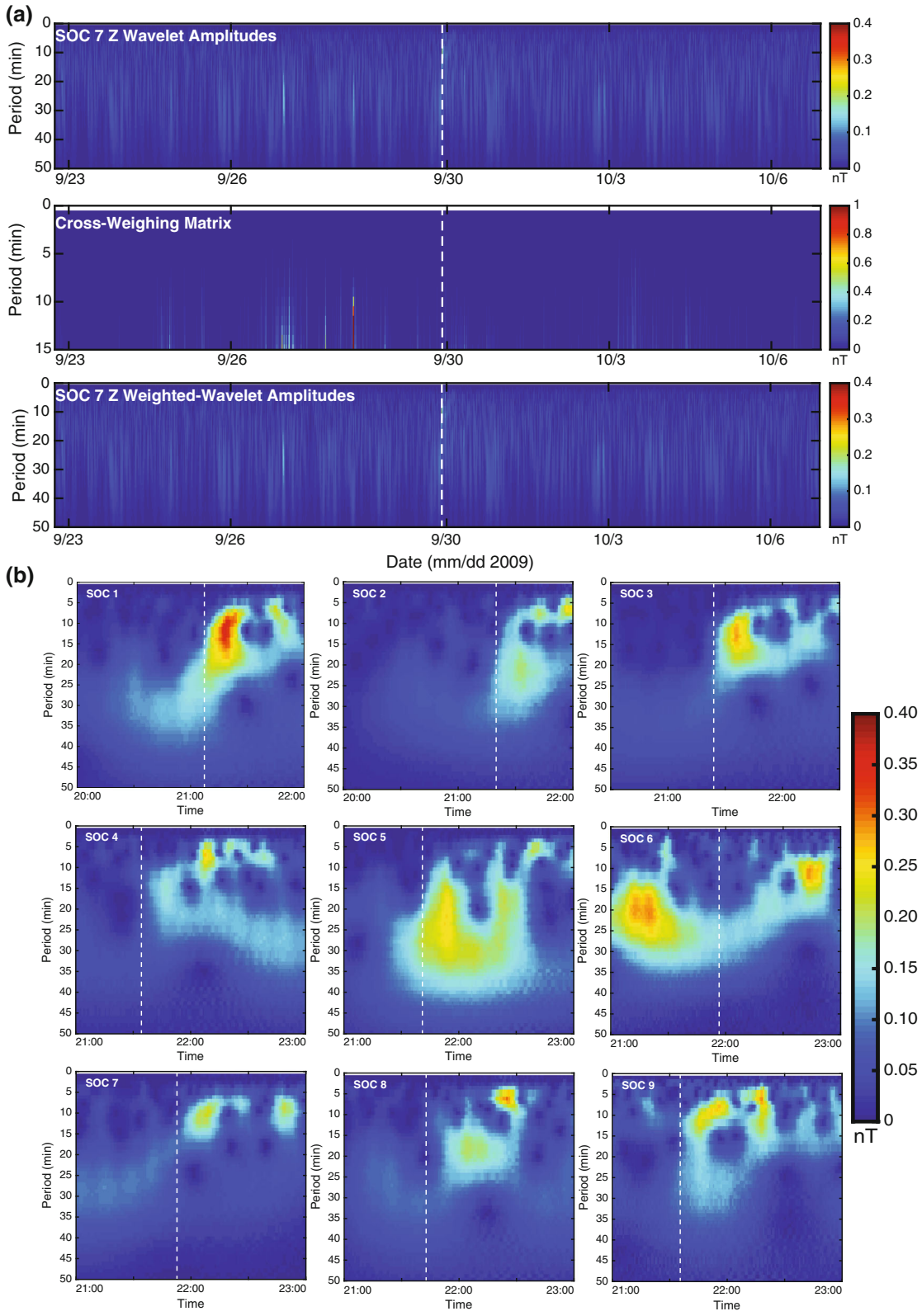
(a)
SOC 7 Z Wavelet Amplitudes
Cross-Weighing Matrix
SOC 7 Z Weighted-Wavelet Amplitudes
Period (min)
9/23
9/26
9/30
10/3
10/6
nT
Date (mm/dd 2009)
(b)
SOC 1
SOC 2
SOC 3
SOC 4
SOC 5
SOC 6
SOC 7
SOC 8
SOC 9
Time
20:00
21:00
22:00
23:00
0.40
0.35
0.30
0.25
0.20
0.15
0.10
0.05
0

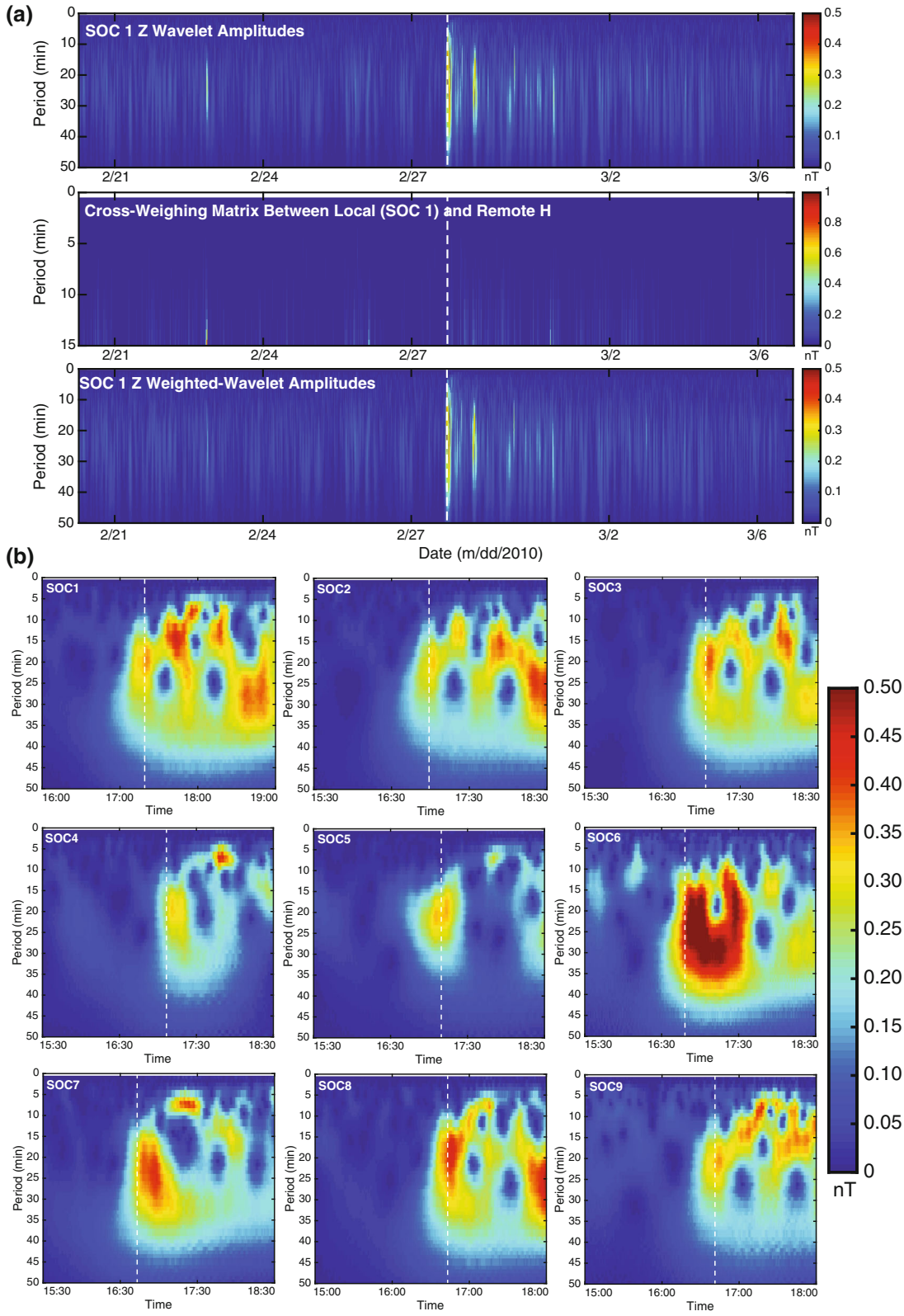
(a)
SOC 1 Z Wavelet Amplitudes
Cross-Weighing Matrix Between Local (SOC 1) and Remote H
SOC 1 Z Weighted-Wavelet Amplitudes
Period (min)
nT
2/21
2/24
2/27
3/2
3/6
Date (m/dd/2010)
(b)
SOC1
SOC2
SOC3
SOC4
SOC5
SOC6
SOC7
SOC8
SOC9
Time
Period (min)
nT

◀Figure 12
Results of the cross-wavelet analysis at the nine SOC stations for the 2010 Chilean event. The *white dashed line* marks the tsunami's estimated time of arrival and UTC time is used. **a** Each step of the analysis is shown: (*top*) the local vertical wavelet periodogram at SOC 1, (*middle*) the cross-wavelet periodogram between the local and remote (HON) horizontal components, and (*bottom*) the weighted wavelet periodogram for the local vertical component. **b** 3 h time windows of the weighted wavelet periodogram for the local vertical component at each SOC station

encouraging for continuing to study the electromagnetic signals of tsunamis, as well as their potential use in tsunami warning systems.

The present study focused on down-weighting the local noise spectrum with cross-amplitudes and studying the time–frequency characteristics of the residual spectrum. Our cross-wavelet analysis only incorporated the signals' amplitudes–we ignored the phase. To properly reconstruct the tsunami magnetic signals from the periodograms the phase must also be included. Future work should incorporate analyzing the phase component of the tsunami signal. This would then enable direct time series comparison between other studies' results. For instance, Ichihara et al. (2013) used the BIRRP programs' remote reference method (Chave and Thomson 2004) to minimize outside noise. While this method also utilizes the horizontal component of a remote station, the transfer function it produces uses cross-spectra methods rather than cross-wavelet methods. It would be useful for future work to directly compare this method's ability to isolate tsunami magnetic signals.

Acknowledgments

We thank Hisashi Utada (Earthquake Research Institute, University of Tokyo) and Noriko Tada (Japan Agency for Marine-Earth Science and Technology) for providing the data (T18) used in this study. The results presented in this paper rely on the data collected at Chichijima (CBI), Kakioka (KAK), Memambetsu (MMB) and Honolulu (HON). We thank the Japan Meteorological Agency for supporting the operation of CBI, KAK and MMB and the U.S. Geological Survey for supporting the operation of HON. We also thank INTERMAGNET for promoting high standards of magnetic observatory practice (http://www.intermagnet.org). The authors would like to thank CIRES innovative research project 2013 for funding. N.R.S. is grateful to the National Oceanic & Atmospheric Administrations Hollings Scholarship Program and the NSF Graduate Research Fellowship Program for supporting her through this research. N.R.S. would also like to thank Matt Pritchard, Rowena Lohman, Robert Tyler and Takuto Minami for useful discussions. Those interested in data from NWP should contact H. Toh (toh@kugi.kyoto-u.ac.jp). For data from the SOC stations, please contact H. Sugioka (hikari@jamstec.go.jp), and for data from T18, please contact H. Utada (utada@eri.u-tokyo.ac.jp).

Appendix: COMCOT

COMCOT has been used to investigate many other tsunami events, including the 1992 Flores Islands, Indonesia tsunami (Liu et al. 1995), the 2003 Algeria tsunami (Wang and Liu 2005), and the 2004 Indian Ocean tsunami (Wang and Liu 2006). The model builds upon the analytical solutions of Okada (1985) to calculate the seafloor deformation from the fault mechanisms. The fault plane is divided into a certain number of rectangular subfaults and the parameters of each subfault are inputted (i.e. length, width, depth, strike angle, dip angle, rake angle and the amount of slip). The seafloor movement due to each subfault can be calculated assuming an elastic semi-infinite half space earth model. Earthquakes typically occur within seconds, thereby preventing the water column above the deforming seafloor from escaping. Consequently, the model does not account for the time dependence of the earthquake's rupture and instead assumes that it happens instantaneously so that the sea surface mimics the deformation of the seafloor.

The fault plane is the interface between the subducting plate and the overriding plate. The strike direction is used to define strike and the angles of rake and dip. Strike direction is the direction one must face to stand on the top edge of the fault plane with the plane on one's righthand side. From this, θ is the angle measured clockwise from north to the strike direction ($0^\circ \leq \theta \leq 360^\circ$). The dip angle δ is the angle between the horizontal top surface and the fault plane

($0° \leq \delta \leq 90°$). Lastly, the rake angle λ is the angle measured anti-clockwise on the fault plane from the strike direction to the direction of the overriding plate's motion relative to the subducting plate ($-180° \leq \lambda \leq 180°$).

The model is then used to solve the linear shallow water wave equations:

$$\frac{\partial \zeta}{\partial t} + \frac{\partial P}{\partial x} + \frac{\partial Q}{\partial y} = 0 \tag{10}$$

$$\frac{\partial P}{\partial t} + gH\frac{\partial \zeta}{\partial x} = 0 \tag{11}$$

$$\frac{\partial Q}{\partial t} + gH\frac{\partial \zeta}{\partial y} = 0 \tag{12}$$

where ζ denotes the free surface elevation, and P and Q are the volume flux in the x and y directions, respectively (ie. $P = hu$, $Q = hv$). These equations are solved via an explicit leap-frog finite differencing model that uses a staggered-grid scheme and the algorithm is parallelized based on FORTRAN and OpenMPI.

References

An, C. (2015). Inversion of tsunami waveforms and tsunami warning. PhD thesis, Cornell University

Baba, K., Utada, H., Goto, T. N., Kasaya, T., Shimizu, H., & Tada, N. (2010). Electrical conductivity imaging of the Philippine Sea upper mantle using seafloor magnetotelluric data. *Physics of the Earth and Planetary Interiors*, *183*(1–2), 44–62. doi:10.1016/j.pepi.2010.09.010. http://linkinghub.elsevier.com/retrieve/pii/S0031920110001949

Chave, A. D., & Thomson, D. J. (2004). Bounded influence magnetotelluric response function estimation. *Geophysical Journal International*, *157*, 988–1006. doi:10.1111/j.1365-246X.2004.02203.x.

Chave, A. D., Filloux, J. H., & Luther, D. S. (1989). Electromagnetic induction by ocean currents: BEMPEX. *Physics of the Earth and Planetary Interiors*, *53*(3–4), 350–359. doi:10.1016/0031-9201(89)90021-6. http://linkinghub.elsevier.com/retrieve/pii/0031920189900216

Cox, C. S., Filloux, J. H., & Larsen, J. C. (1971). Electromagnetic studies of ocean currents and electrical conductivity below the ocean-floor (pp. 637–693). In *The sea*

Daubechies, I. (1992). Ten lectures on wavelets. In *CBMSNSF regional conference series in applied mathematics* (61st ed.). Philadelphia: SIAM

Denig, W. F. (2015). *Geomagnetic kp and ap indices*. http://www.ngdc.noaa.gov/stp/GEOMAG/kp_ap.html

Fujii, Y., & Satake, K. (2008). Tsunami sources of the November 2006 and January 2007 Great Kuril Earthquakes. *Bulletin of the Seismological Society of America*, *98*(3), 1559–1571. doi:10.1785/0120070221. http://www.bssaonline.org/cgi/

Fujii, Y., & Satake, K. (2009). *Samoa Islands Tsunami on Sep. 29, 2009*. http://iisee.kenken.go.jp/staff/fujii/Samoa/tsunami.html

GEBCO (2013) The GEBCO_08 grid, version 20100927. Tech. rep., general bathymetric chart of the oceans. http://www.gebco.net

González, F. I., & Kulikov, Y. A. (1993). Tsunami dispersion observed in the deep-ocean. In S. Tinti (Ed.), *Tsunamis in the world* (pp. 7–16). The Netherlands: Kluwer.

González, F. I., Satake, K., Boss, E. F., & Mofjeld, H. O. (1995). Edge wave and non-trapped modes of the 25 April 1992 Cape Mendocino Tsunami. *Pageoph*, *144*, 18.

Grossmann, A., & Morlet, J. (1984). Decomposition of hardy functions into square integrable wavelets of constant shape. *SIAM Journal on Mathematical Analysis*, *15*(4), 723–736.

Gutenberg, B., & Richter, C. F. (1956). Earthquake magnitude, intensity, energy, and acceleration. *Annals of Geophysics*, *9*(1), 15.

Ichihara, H., Hamano, Y., Baba, K., & Kasaya, T. (2013). Tsunami source of the 2011 Tohoku earthquake detected by an ocean-bottom magnetometer. *Earth and Planetary Science Letters*, *382*, 117–124. doi:10.1016/j.epsl.2013.09.015

Klausner, V., Mendes, O., Domingues, M. O., Papa, A. R. R., Tyler, R. H., Frick, P., et al. (2014). Advantage of wavelet technique to highlight the observed geomagnetic perturbations linked to the Chilean tsunami (2010). *Journal of Geophysical Research: Space Physics*, *119*(2010), 1–17. doi:10.1002/2013JA019398.

Larsen, J. C. (1968). Electric and magnetic fields induced by deep sea tides. *The Geophysical Journal of the Royal Astronomical Society*, *16*, 47–70.

Larsen, J. C. (1991). Transport measurements from in-service undersea telephone cables. *IEEE Journal of Oceanic Engineering*, *16*(4), 313–318. doi:10.1109/48.90893. http://ieeexplore.ieee.org/lpdocs/epic03/wrapper.htm?arnumber=90893

Larsen, J. C., & Sanford, T. B. (1985). Florida current volume transports from voltage measurements. *Science*, *227*(4684), 302–304.

Liu, P. C. (2000). Wavelet transform and new perspective on coastal and ocean engineering data analysis. In *Advances in coastal and ocean engineering* (pp 57–99) Singapore: World Scientific Publishing Co

Liu, P. L. F., Cho, Y. S., Briggs, M. J., Kanoglu, U., & Synolakis, C. E. (1995). Runup of solitary waves on a circular island. *Journal of Fluid Mechanics*, *302*, 259–285.

Malin, S. R. C. (1970). Separation of lunar daily geomagnetic variations into parts of ionospheric and oceanic origin. *The Geophysical Journal of the Royal Astronomical Society*, *21*, 447–455.

Manoj, C., Maus, S., & Chulliat, A. (2011). Observation of magnetic fields generated by tsunamis. *Eos*, *92*(2), 13–14. doi:10.1126/science.

Maus, S., & Kuvshinov, A. (2004). Ocean tidal signals in observatory and satellite magnetic measurements. *Geophysical Research Letters*, *31*, L15313. doi:10.1029/2004GL020090. http://www.agu.org/pubs/crossref/2004/2004GL020090.shtml

McKnight, J. D. (1995). Lunar daily geomagnetic variations in New Zealand. *Geophysical Journal International*, *122*, 889–898.

Mendes, O., Domingues, M. O., Mendes da Costa, A., & Clua de Gonzalez, A. L. (2005). Wavelet analysis applied to

magnetograms: Singularity detections related to geomagnetic storms. *Journal of Atmospheric and Solar-Terrestrial Physics*, *67*, 1827–1836. doi:10.1016/j.jastp.2005.07.004.

Minami, T., Toh, H., & Tyler, R. H. (2015). Properties of electromagnetic fields generated by tsunami first arrivals: Classification based on the ocean depth. 30, 1092 42:2171–2178. doi:10.1002/2015GL063055

Mofjeld, H. O., González, F. I., & Newman, J. C. (1997). Short-term forecasts of inundation during teletsunamis in the eastern North Pacific Ocean. In G. Hebenstreit (Ed.), *Perspectives on tsunami hazard reduction* (pp. 145–155). Amsterdsam: Kluwer Acad.

Nagarajan, B., Suresh, I., Sundar, D., Sharma, R., Lal, A. K., Neetu, S., et al. (2006). The great tsunami of 26 December 2004: A description based on tide-gauge data from the Indian subcontinent and surrounding areas. *Earth Planets Space*, *58*, 211–215.

Newland, D. E. (1993). Harmonic wavelet analysis. *Proceedings of the Royal Society*, *443*(1917), 203–225. doi:10.1098/rspa.1993.0140. http://rspa.royalsocietypublishing.org/cgi/

NOAA (2015) Global historical tsunami database. Tech. rep., National Geophysical Data Center / World Data System (NGDC/WDS), Boulder. http://www.ngdc.noaa.gov/hazard/tsu_db.shtml

Okada, Y. (1985). Surface deformation due to shear and tensile faults in a half-space. *Bulletin of the Seismological Society of America*, *75*(4), 1135–1154.

Rabinovich, A. B., & Thomson, R. E. (2007). The 26 December 2004 Sumatra Tsunami: Analysis of tide gauge data from the world ocean Part 1. Indian Ocean and South Africa. *Pure and Applied Geophysics*, *164*(2–3), 261–308. doi:10.1007/s00024-006-0164-5. http://link.springer.com/

Rabinovich, A. B., Thomson, R. E., & Stephenson, F. E. (2006). The Sumatra tsunami of 26 December 2004 as observed in the North Pacific and North Atlantic oceans. In *Surveys in geophysics* (vol. 27, pp. 647–677). doi:10.1007/s10712-006-9000-9. http://link.springer.com/10.1007/s10712-006-9000-9

Sanford, T. B. (1971). Motionally induced electric and magnetic fields in the sea. *Journal of Geophysical Research*, *76*(15). doi:10.1029/JC076i015p03476. http://www.agu.org/pubs/crossref/1971/JC076i015p03476.shtml

Schnepf, N. R., Manoj, C., Kuvshinov, A., Toh, H., & Maus, S. (2014). Tidal signals in ocean bottom magnetic measurements of the Northwestern Pacific: Observation versus prediction. *Geophysical Journal International*, *198*(2), 1096–1110.

Suetsugu, D., Shiobara, H., Sugioka, H., Ito, A., Isse, T., Kasaya, T., Tada, N., Baba, K., Abe, N., Hamano, Y., Tarits, P., Barriot, J. P., & Reymond, D. (2012). TIARES project—Tomographic investigation by seafloor array experiment for the Society hotspot. *Earth, Planets and Space64*(4), i–iv. doi:10.5047/eps.2011.11.002

Sugioka, H., Hamano, Y., Baba, K., Kasaya, T., Tada, N., & Suetsugu, D. (2014). Tsunami: Ocean dynamo generator. Nature Scientific reports 4. doi:10.1038/srep03596. http://www.pubmedcentral.nih.gov/articlerender.fcgi?artid=3884372&tool=pmcentrez&rendertype=abstract

Tang, L., Titov, V. V., Wei, Y., Mofjeld, H. O., Spillane, M., Arcas, D., et al. (2008). Tsunami forecast analysis for the May 2006 Tonga tsunami. *Journal of Geophysical Research*, *113*(C12), C12015. doi:10.1029/2008JC004922

Tatehata, H., Ichihara, H., & Hamano, Y. (2015). Tsunami-induced magnetic fields detected at Chichijima Island before the arrival of the 2011 Tohoku earthquake tsunami. *Earth, Planets and Space*, *67*(185). doi:10.1186/s40623-015-0347-3

Thomson, D. J., Lanzerotti, L. J., Maclennan, C. G., & Medford, L. V. (1995). Ocean cable measurements of the tsunami signal from the 1992 Cape Mendocino earthquake. *Pure and Applied Geophysics*, *144*(3–4), 427–440. doi:10.1007/BF00874376. http://www.springerlink.com/index/

Titov, V., Rabinovich, A. B., Mofjeld, H. O., Thomson, R. E., & González, F. I. (2005). The global reach of the 26 December 2004 Sumatra Tsunami. *Science*, *309*(5743), 2045–2048.

Toh, H., Hamano, Y., & Ichiki, M. (2006). Long-term seafloor geomagnetic station in the northwest Pacific : A possible candidate for a seafloor geomagnetic observatory. *Earth Planets Space*, *58*, 697–705.

Toh, H., Satake, K., Hamano, Y., Fujii, Y., & Goto, T. (2011). Tsunami signals from the 2006 and 2007 Kuril earthquakes detected at a seafloor geomagnetic observatory. *Journal of Geophysical Research*, *116*(B2), B02104. doi:10.1029/2010JB007873. http://doi.wiley.com/

Tyler, R. H. (2005). A simple formula for estimating the magnetic fields generated by tsunami flow. *Geophysical Research Letters*, *32*(9), 1–4. doi:10.1029/2005GL022429. http://www.agu.org/pubs/crossref/2005/2005GL022429.shtml

Tyler, R. H., Maus, S., & Lühr, H. (2003). Satellite observations of magnetic fields due to ocean tidal flow. *Science*, *299*(5604), 239–241. doi:10.1126/science.1078074. http://www.ncbi.nlm.nih.gov/pubmed/12522247

Utada, H., Shimizu, H., Ogawa, T., Maeda, T., Furumura, T., Yamamoto, T., et al. (2011). Geomagnetic field changes in response to the 2011 off the Pacific Coast of Tohoku Earthquake and Tsunami. *Earth and Planetary Science Letters*, *311*(1–2), 11–27.

Wang, X., & Liu, P. L. F. (2006). An analysis of 2004 Sumatra earthquake fault plane mechanisms and Indian Ocean tsunami. *Journal of Hydraulic Research*, *44*(2), 147–154.

Wang, X. M., & Liu, P. L. F. (2005). A numerical investigation of Boumerdes–Zemmouri (Algeria) earthquake and tsunami. *CMES—Computer Modeling In Engineering & Sciences*, *10*(2), 171–183.

Yue, H., Lay, T., Rivera, L., An, C., Vigny, C., & Tong, X. (2014). Localized fault slip to the trench in the 2010 Maule, Chile Mw=8.8 earthquake from joint inversion of high-rate GPS, teleseismic body waves, InSAR, campaign GPS, and tsunami observations. *Journal of Geophysical Research: Solid Earth*, *119*, 7786–7804. doi:10.1002/2014JB011340.Received.

Zhang, L., Baba, K., Liang, P., Shimizu, H., & Utada, H. (2014). The 2011 Tohoku Tsunami observed by an array of ocean bottom electromagnetometers. *Geophysical Research Letters*, *41*, 4937–4944. doi:10.1002/2014GL060850.

(Received January 15, 2016, revised June 27, 2016, accepted June 29, 2016, Published online July 15, 2016)